Journal of Alloys and Compounds 994 (2024) 174720

Contents lists available at ScienceDirect

Journal of Alloys and Compounds

journal homepage: www.elsevier.com/locate/jalcom

A comparative study on the production of $Ni_{1/3}Co_{1/3}Mn_{1/3}C_2O_4$ cathode precursor material for lithium-ion batteries using batch and slug-flow reactors

Jethrine H. Mugumya, Sourav Mallick, Arjun Patel, Michael L. Rasche, Aardra V. Sakpal, Ethan D. Huchler, Sunuk Kim, Ram B. Gupta *, Mo Jiang *

Department of Chemical and Life Science Engineering, Virginia Commonwealth University, Richmond, VA 23219, USA

ARTICLE INFO

Keywords:
Batch reactor
Cathode
Lithium-ion battery
Oxalate co-precipitation
Slug-flow reactor

ABSTRACT

The intermittent nature of the renewable energy sources drifts research interest towards various electrochemical energy storage devices, such as the lithium ion battery, which offers consistent power supply. The manufacturing cost and electrochemical performance of a battery pack largely depends on the quality of the cathode material, which further depends on the production method and its parameters. However, the traditional stirred tank-based co-precipitation manufacturing process for precursors of lithium nickel manganese cobalt oxide (NCM111) cathode suffers from inhomogeneity in the reaction environment, which leads to non-uniform morphology and particle size distribution (PSD). In this work, slug-flow-based manufacturing platform, which offers a homogeneous reaction environment, is used for the continuous production of NCM111 oxalate precursors. One of the novel features of this work is the comparative study between the quality of batch and slug-flow-derived products. The slug-flow-derived product is found to be better in terms of having bigger particle size, narrower PSD and higher tap density. The study on the single and dual-element precipitation in similar conditions to understand the co-precipitation behavior in the slug-flow manufacturing platform is also a unique feature of this work. Furthermore, the effect of NH_4OH concentration and residence time (RT) on the electrochemical performance of cathode were also studied and it is found that the cathode precursors synthesized at a NH_4OH concentration of 0.08 M and a RT of 2 minutes followed by lithiation shows a better electrochemical performance of 128 mAh g^{-1} at 0.1 C with cycling stability of more than 80% both at 0.5 C and 1 C.

1. Introduction

Energy density, cycle life, and capacity are some of the parameters considered when selecting lithium ion batteries for various applications such as electric vehicles, electronics, and electric grid applications [1–3]. As the cathode is the major contributor in terms of overall cost and weight of the lithium ion battery, it has a key role in determining the capacity and energy density of the battery [4,5]. Layered metal oxides such as Lithium Nickel Cobalt Manganese oxide (NCM) or Lithium Nickel Cobalt Aluminum oxide (NCA) are most popular materials in the research and commercial spaces due to their high specific capacity and energy density in comparison to other cathode materials [6].

Among the various synthesis methods for NCM production, co-precipitation of the precursor material followed by lithiation is a well-established synthesis method commercially and it is commonly applied in the production of NCM-based cathodes [7]. First, precursor synthesis of $Li(Ni_{1/3}Mn_{1/3}Co_{1/3})O_2$ or NCM111 is typically carried out in tank based reactors (batch or stirred tank) [8–10]. The reactants are loaded via one input point of the vessel and left for a reaction (residence) time of hours for particle nucleation and growth [10–12], while a stirrer is mixing all the reactants in the reactor. The precursor is then collected and analyzed to assess the quality of the precursor before moving to the lithiation step. Tank-based reactors are widely adopted and are a popular synthesis choice due a number of reasons such as [13,14] (i) established regulatory framework for product quality of batch-derived products that has remained unchanged for a long time hence resistance to alter reactor setup, (ii) established fact that batch process can be scaled up from bench top to large scale production, (iii) minimal cost of production associated with batch reactors, (iv) flexibility of tank based reactors to produce a range of products such as pharmaceuticals, food

---

* Corresponding authors.
E-mail addresses: rbgupta@vcu.edu (R.B. Gupta), mjiang3@vcu.edu (M. Jiang).

https://doi.org/10.1016/j.jallcom.2024.174720
Received 29 February 2024; Received in revised form 12 April 2024; Accepted 1 May 2024

products and battery materials. Although tank-based reactors are the preferred reactor type, they have a number of challenges. One main issue is the inhomogeneous microenvironment at different points inside the reactor that make it harder to achieve product uniformity. Another issue is the production rate that is limited by the reactor size therefore multiple rounds of batch synthesis are required to get a large quantity product. Furthermore, variation in product quality can emerge from the slightest change in process parameters when switching out batches. One possible solution to improve the product quality is maintaining homogeneous microenvironment throughout the reactor, which can be achieved using a continuous reactor.

Slug flow reactors fall under the continuous reactor class, which are known for improved process control and better product quality. A slug flow reactor is a tubular type of continuous reactor in which slugs act as microliter batch reactors and experience the same microenvironment resulting in enhanced product quality. The formation of slugs (segments) in the reactor depends on factors like flowrate, tube diameter, and fluid properties [15]. Based on different transport parameters, liquid and gas phases can form a variety of flow patterns (regimes) such as bubble flow, churn flow, annular flow, and slug flow [16,17]. Out of these patterns, the slug flow pattern, where liquid slugs are completely separated by gas segments, can be used to carry out the co-precipitation reaction to produce NCM precursors. The slug flow regime is preferred over other flow regimes because of two major reasons. The first reason is the reduced contact between the liquid (reaction volume) and tubing walls resulting in a lesser possibility of clogging due to the affinity of crystals to the wall. Secondly, each of the liquid slugs has good internal circulation which results in excellent mixing throughout the whole microliter reactor [18,19]. In addition to good mixing inside each slug, some of the other benefits of using a slug flow reactor are; (i) continuous production regardless of the reactor size, (ii) reactant addition can easily be controlled, (iii) uniform microenvironments throughout the reactor once steady state is achieved. These characteristics enable the slug-flow reactors suitable candidates for the co-precipitation of pure NCM-based cathode precursors. As per our knowledge, there is currently no literature on the flow synthesis of NCM111 precursors.

Co-precipitation of the NCM111 hydroxide precursor has been widely studied and optimized [11,20,21]. Compared to hydroxide synthesis, there are less reports on co-precipitation of NCM111 as oxalate. [22,23] Hydroxide co-precipitation is preferred due to a homogeneous distribution of transition elements and a higher tap-density particle. However, the reaction is sensitive to pH and it needs an inert environment to avoid manganese oxidation. On the contrary, oxalate co-precipitation is less sensitive to pH change, can be carried out at a much more neutral pH (7−8) and it has less sensitivity to air environment. This makes it a preferable precipitating agent for the slug flow synthesis of NCM-precursor particles. Hence, the evaluation of the oxalate precipitation kinetics of the three elements is crucial to understand the compositional variation of the slug-flow-derived precursor at different reaction conditions. In addition to a transition metal salt solution, the other two reactants used for NCM111 oxalate co-precipitation are ammonium hydroxide (NH_4OH) and an oxalate salt (oxalic acid or ammonium oxalate) solutions. [24–26] The NH_4OH concentration plays an important role in the precipitation of the tri-metallic oxalate as both cation (NH_4^+) and anion (OH^-) influence the reaction. The amine ion can act as a chelating agent and form a complex with the three metal ions. This complex reacts with the oxalate anion in solution to form the precipitate. Meanwhile the hydroxide ion maintains the pH of the reaction around 8 which is conducive for the NCM111 oxalate precipitation. [3] Varying the NH_4OH concentration will affect the composition and particle size of the synthesized NCM111 oxalate. In addition, residence time is another key parameter that influences particle formation and growth. Particle size and composition are some of the properties that influence electrochemical performance so it is important to evaluate parameters that affect these properties.

One of the main benefits of using co-precipitation synthesis is the ability to tune the composition of the precursor. However not all reaction conditions result in a precursor product with the same stoichiometry as the feed solution. Some work has been done by other groups using a batch reactor to study the precipitation behavior of some of the transition elements separately such as a Ni/Mn oxalate system or a Ni/Co oxalate system [7,27]. Although, in these cases, the final target was not to understand the precipitation behavior of all three transition elements (Ni, Mn and Co) during precipitation of the tri-metallic oxalate. In that regard, to understand the precipitation behavior of the three transition elements in the slug-flow reactor, single and dual element experiments are also performed. The NCM111 oxalate produced from the slug-flow reactor is then compared to the batch-derived product. As both oxalates are synthesized using similar reaction conditions, we evaluate the precursor quality in terms of particle homogeneity, tap density, elemental distribution and electrochemical performance. An experimental study is then conducted to evaluate the optimal reaction conditions for the slug flow reactor by varying the chemical (NH_4OH concentration) as well as flow (residence time) parameters. Finally, the electrochemical performance of the slug-flow derived NCM111 are evaluated in terms of specific capacity, cycling stability, rate capability, electrode polarization and impedance behavior.

2. Experiments

2.1. Materials and synthesis

Nickel sulfate hexahydrate ($NiSO_4.6\ H_2O$), cobalt sulfate heptahydrate ($CoSO_4.7\ H_2O$) and manganese sulfate monohydrate ($MnSO_4{\cdot}H_2O$), all purchased from Sigma Aldrich, are used to prepare a 0.2 M transition metal ion sulfate solution (MSO_4) in a stoichiometric ratio. In addition, ammonium oxalate solution (($(NH_4)_2C_2O_4$, 0.2 M) and ammonium hydroxide solution (NH_4OH) of the desired concentration are also prepared. The experiments are carried out in the batch and slug-flow reactors, with the equation for the precipitation reaction shown in the following equations. [3]

$$M^{2+} + xNH_4OH\ (aq) \rightarrow M(NH_3)_n^{2+}\ (aq) + xH_2O(aq) \tag{1}$$

$$M(NH3)_n^{2+}\ (aq) + yC_2O_4^{2-} \rightarrow MC_2O_4 + nH_2O \tag{2}$$

The obtained precursor product, ($Ni_{1/3}Mn_{1/3}Co_{1/3}C_2O_4$) or oxalate precursor, is then washed, filtered and subsequently dried at 90 °C overnight. The precursors produced at different ammonium hydroxide concentrations and residence time conditions are labeled as NCM (OX)-z (z = the molar concentration of ammonium hydroxide; 0.05, 0.08, 0.1, and 0.2) and NCM (OX)-Ry (Ry = the residence time; 2, 4 and 8 minutes). The dried powder is then mixed with 5 wt% excess lithium hydroxide and calcined at 850°C for 12 h to produce $Li(Ni_{1/3}Mn_{1/3}Co_{1/3})O_2$ (NCM111). When calcining the oxalate precursor, slow heating rate of 0.5 °C/min is utilized in order to retain morphology of the particles after calcination. The resulting NCM111 samples based on the corresponding reaction conditions are labelled as follows: NCM-z (z = the molar concentration of ammonium hydroxide; 0.05, 0.08, 0.1 and 0.2) and NCM-Ry (Ry = the residence time; 2, 4 and 8 minutes).

2.2. Co-precipitation reactors

2.2.1. Slug-flow reactor

The slug flow reactor consists of four syringe pumps (New Era Pump Systems, Model NE-1000), a mass flow controller (Omega Engineering, FMA-2617A), heating apparatus/oven (VWR Mini-incubator, 97025–630) to maintain reaction temperature inside the slugs at 35°C, fluorinated ethylene propylene (FEP) tubing (Grainger, 3/32 I.D.) and a filtration unit to collect the product. The reactor set-up is shown in Fig. 1. Three phase slug flow which consists of liquid-liquid-gas slugs is used for this precipitation reaction in order to prevent fouling and clogging. [18,28] First, the mineral oil was fed using a syringe pump as

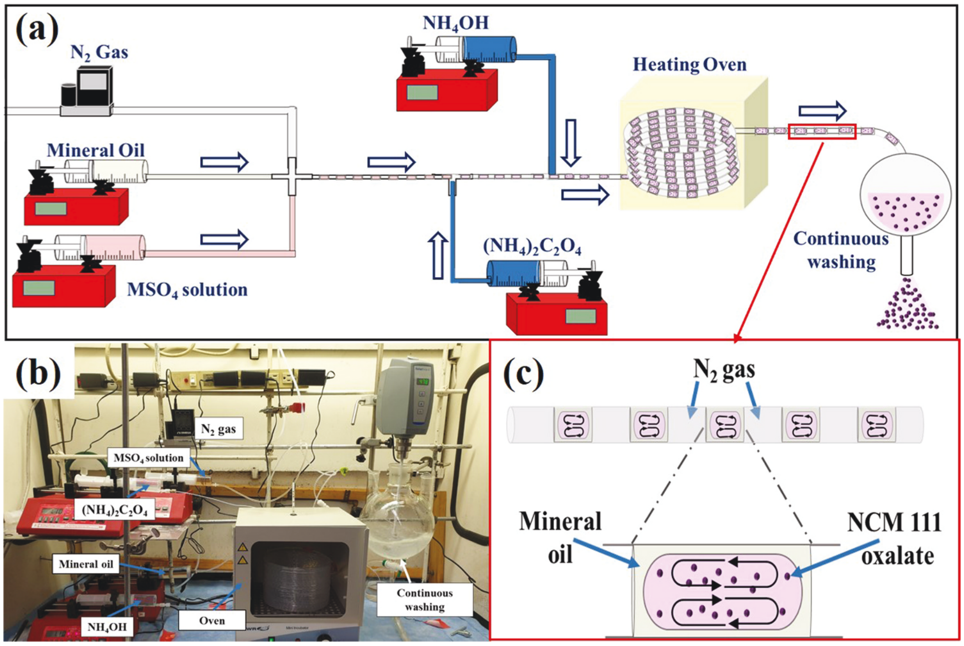

Fig. 1. (a) Schematic illustration and (b) digital image of the slug flow reactor. (c) Schematic representation of the internal circulation inside a slug of the three-phase slug-flow.

the continuous phase to lubricate the tubing, together with nitrogen gas, which was regulated using a mass flow controller. The metal ion solution was then added to the oil/N$_2$ stream via the tee-connector. Aqueous solutions of $(NH_4)_2C_2O_4$ and NH_4OH were then fed sequentially through two feeding points and the flow rates were adjusted in such a way that the reagents would thoroughly mix with the aqueous slugs containing MSO_4. The slugs were allowed to stay for a specific residence time in the oven and then collected in a separation vessel filled with de-ionized water. This quenches the reaction and washes the product simultaneously to remove mineral oil. Corresponding volumes and flow rates of the feed streams are shown in Table 1.

2.2.2. *Batch reactor*

The transition metal sulfate solution (0.2 M) was added to a three neck round bottomed flask filled with nitrogen gas and the temperature inside the reactor adjusted to 35°C (which matches the temperature of the liquid slugs). $(NH_4)_2C_2O_4$ (0.2 M) followed by NH_4OH (0.1 M) solution were then poured into the metal sulfate solution. The reaction was allowed to run for 4 minutes and the precipitate was collected and washed before drying it overnight at 90°C. It is worth mentioning that, in-order to compare the quality of the batch and slug-flow products, similar reaction conditions including, reagent concentration, reaction time and temperature are maintained during the batch synthesis.

2.3. *Material characterizations*

Particle morphology and particle size distribution is studied using electron microscopy (SEM, Hitachi SU-700) equipped with Energy Dispersive Spectroscopy (EDS) for elemental mapping of the samples.

Table 1
Slug-flow parameters for oxalate co-precipitation reaction.

Feed	Flow rate	Volume(ml)
MSO_4	1.00 ml/min	50
NH_4OH	1.10 ml/min	60
$(NH_4)_2C_2O_4$	1.10 ml/min	60
Mineral Oil	0.95 ml/min	As required
Nitrogen	10.50 SCCM	–

Inductively coupled plasma optical emission spectrometry (ICP-OES, 5110, Agilent Technologies) is used to determine the chemical composition of the oxalate precursor samples. The crystallography of the samples is analyzed using X-ray diffraction, XRD, (Empyrean Multipurpose Diffractometer) with a Cu Kα radiation source of wavelength of 1.5406 Å. The XRD patterns are collected on a 2θ range of 10–80°. Rietveld refinement of the XRD patterns of lithiated NCM111 is carried out using the High Score Software from Panalytical. Thermal gravimetric analysis is carried out using TGA Q500 (TA instruments) with a ramp rate of 10°C min^{-1}. X-ray Photoelectron Spectroscopy (XPS) is performed using Phi Versa Probe III Scanning XPS Microprobe.

2.4. *Electrochemical measurements*

NCM111 is first mixed with carbon black (Super P conductive carbon black, MSE Supplies) and polyvinylidene difluoride (PVDF, HSV 900) binder in N-methyl pyrrolidone solvent (NMP, 99.5% anhydrous, Sigma Aldrich) in a weight ratio of 8:1:1. Then resulting slurry is then coated onto aluminum foil using the doctor blade method and then vacuum dried at 130°C overnight. To prepare the coin cells in an inert atmosphere, the electrodes are then punched into discs and moved to the glove box with an environment of less than 0.5 ppm of water and oxygen. CR-2032 type coin cells are used for electrochemical testing with lithium foil as the anode, 1 M $LiPF_6$ in ethylene carbonate/dimethyl carbonate [EC/DMC = 50:50 (v/v)] as the electrolyte and Celgrade 2340 tri-layer microporous membrane as the separator. Galvanostatic charge/discharge tests are performed using MTI battery test cycler and Arbin LBT20084 battery tester. Rate capability and cycling stability are carried out at different C-rates (1 C = 200 mAh g^{-1}) within the voltage range of 2.7–4.3 V (vs. Li/Li^{+}). Electrochemical impedance spectroscopy (EIS) measurements are performed using a Gamry potentiostat interface 5000E with an amplitude of 5 mV within a frequency range from 100 kHz to 10 mHz. All the electrochemical tests are performed at room temperature.

3. Results and discussion

3.1. Comparison of product quality between batch and slug-flow reactors

For the comparison experiments of the tri-metallic oxalate co-precipitation in the batch and slug-flow reactor systems, similar reaction conditions are used (MSO_4 concentration of 0.2 M, $(NH_4)_2C_2O_4$ concentration of 0.2 M, NH_4OH concentration of 0.1 M, residence time of 4 minutes).

The morphology of the oxalate particles derived from the slug flow and batch reactors are shown in Fig. 2 and Fig. S1. In all the cases, nano-sized primary particles accumulated to form micro-sized secondary particles. Batch derived oxalate (Fig. 2a and Fig. 2c) is composed of highly agglomerated secondary particles with quasi-spherical morphology; whereas slug flow derived oxalate (Fig. 2b and Fig. 2d) has spherical secondary particles with minimal agglomeration. Oxalate precursors from both reactor systems have needle shaped primary particles as observed in Fig. 2c and Fig. 2d. Average particle size of all the precursors are shown in Fig. 2e. The slug-flow reactor produced bigger particles with an average size of 7.9 μm compared to the batch-derived oxalate that has an average particle size of 6.6 μm. However, from the co-efficient of variation (CV) values of the two-oxalate samples, we observed that the batch derived oxalate had a wider particle size distribution (0.24) compared to the slug-flow derived product (0.13). The homogeneity in particle size distribution is one of the primary advantages of slug flow reactor compared to batch.

Although similar reaction parameters are maintained in both reactors, the dissimilarity in the particle size and particle size distribution is caused due to the differences in the local reaction environments inside the two reactors. In a stirred tank reactor, as particles circulate through the reaction mixture, they are likely to break due to collision with the impeller or splinter in the high shear region of the vortices of the impeller [19,29]. This reduces the size of these particles and the resulting fragments are either consumed by the surrounding particles or become seeds for secondary nucleation. This results in smaller size particles with a wide particle size distribution, which further supports the observations from the batch precursor synthesis. Conversely with a slug flow reactor, due to the absence of an impeller there is minimal attrition that would reduce particle size and induce secondary nucleation [15,30,31]. In addition, unlike a stirred tank reactor that has an inconsistent temperature profile, the micro-sized scale of each slug facilitates uniform heat transfer which is further enhanced through internal circulation [32,33]. As such, each particle inside a single slug experiences the similar reaction environment and with slug uniformity, particles in adjacent slugs will develop in a similar environment [34,35]. The uniform environment in each slug and between adjacent slugs is conducive for the nucleation and growth of similar-sized particles hence the narrow particle size distribution observed in the slug-flow derived oxalate.

Secondary particles from both batch and slug-flow derived precursors are mechanically cut and cross-sectional line mapping is carried out to examine the distribution of the metal ions. For batch derived oxalate particles (Fig. 3a), the concentration of the metal ions is higher around the edges of the particle. On the other hand, for the slug-flow derived oxalate particles (Fig. 3b), the metal ions are more concentrated at the core. This indicates that the batch oxalate particles are less dense than the slug-flow synthesized oxalate particles. This is further validated with tap density measurements as the slug flow precursor had a higher tap density of 0.80 g ml^{-1} than the batch precursor with a tap density of 0.49 g ml^{-1}. A similar trend of tap density is also observed after lithiating the materials. The SEM images of the lithiated materials are shown in Fig S2.

TGA profiles for both oxalate samples are shown in Fig. S3. Both oxalate precursors exhibit a similar decomposition profile that involves two steps. The first step involves dehydration of the metal oxalate, which occurs in a temperature range of 150 °C to 200 °C. Both oxalates lose about 17–19 % of their initial weight which is close to the theoretical weight loss (19.8 %), indicating both oxalates contain 2 moles of crystal water [22]. The second weight loss transpires between 250 °C to 300 °C, corresponding to the decomposition of the anhydrous metal oxalate into metal oxide and gases (e.g. CO and CO_2). These reactions are summarized in the equations below.

$$Ni_{1/3}Co_{1/3}Mn_{1/3}C_2O_4.2H_2O\ (s) \rightarrow Ni_{1/3}Co_{1/3}Mn_{1/3}C_2O_4\ (s) + 2H_2O\ (g) \quad (3)$$

$$3(Ni_{1/3}Co_{1/3}Mn_{1/3})C_2O_4\ (s) + 2O_2\ (g) \rightarrow (Ni_{1/3}Co_{1/3}Mn_{1/3})_3O_4\ (s) + 6CO_2\ (g) \quad (4)$$

3.2. Effect of slug-flow reaction conditions on particle properties

3.2.1. Effect of NH_4OH concentration on NCM111 particle properties

Four different NCM111 oxalate precursor samples are prepared in a slug-flow reactor with a fixed concentration of MSO_4 and $(NH_4)_2C_2O_4$ (0.2 M) while varying the feeding concentration of NH_4OH at a fixed residence time of 4 minutes. There was a minimal pH variation observed with change in the ammonium hydroxide concentration. Fig. 4a – Fig. 4h shows the SEM images of low and high magnifications of the synthesized NCM oxalate precursors. All the particles of the four samples have a morphology of micron-sized secondary particles composed of nano-sized primary particles. In Fig. 4(e), NCM(Ox)-0.05 has plate like primary particles while the secondary particle morphology is cuboidal. The rest of the samples have needle-shaped primary particles and spherical secondary particles. The effect of the NH_4OH concentration variation on the particle size is illustrated in Fig. 4(i). As the concentration increased from 0.05 M to 0.08 M, there was an increase in average particle size

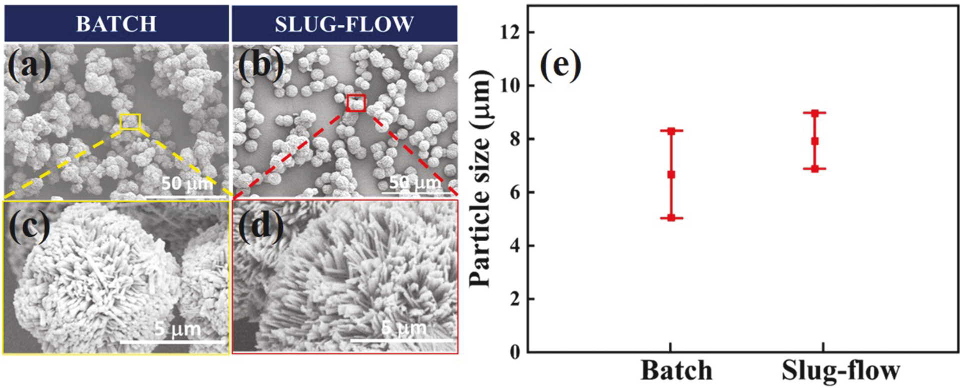

Fig. 2. SEM images of NCM111 oxalate particles derived from (a,c) batch reactor and (b,d) slug-flow reactor at different magnification. (e) Average particle size of batch and slug-flow derived precursors.

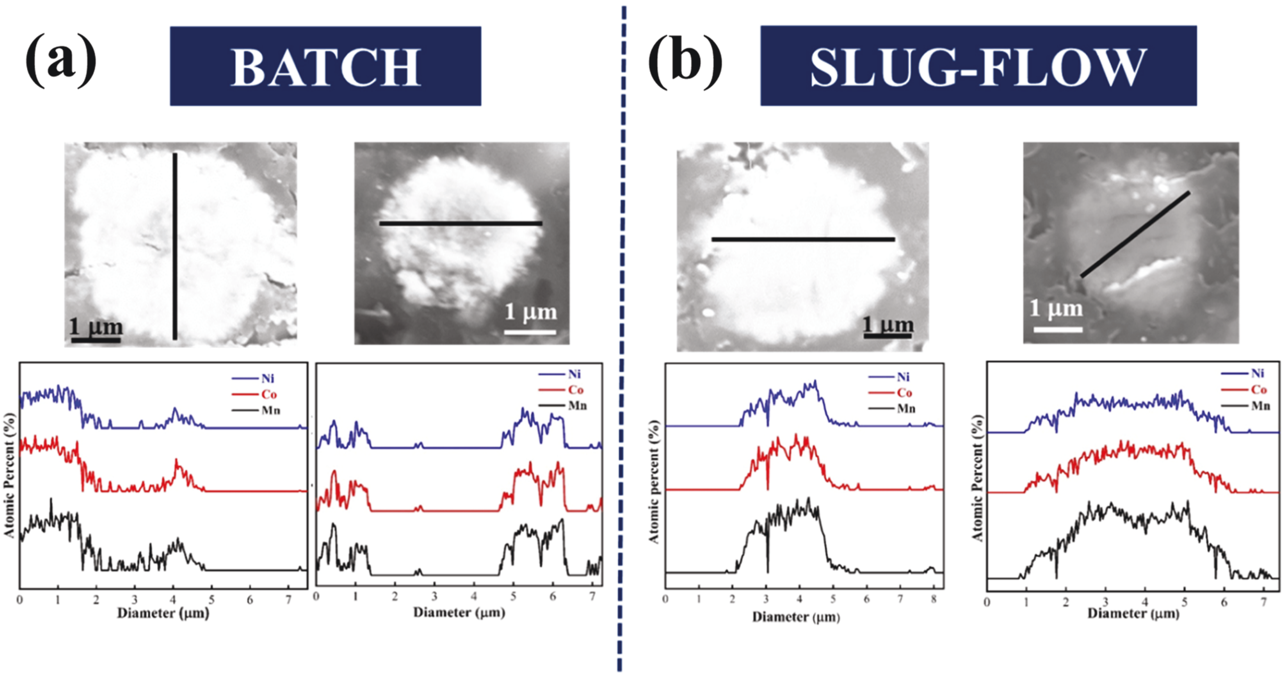

Fig. 3. Cross-sectional EDS line mapping profile of the oxalate particles of (a) batch and (b) slug-flow reactor.

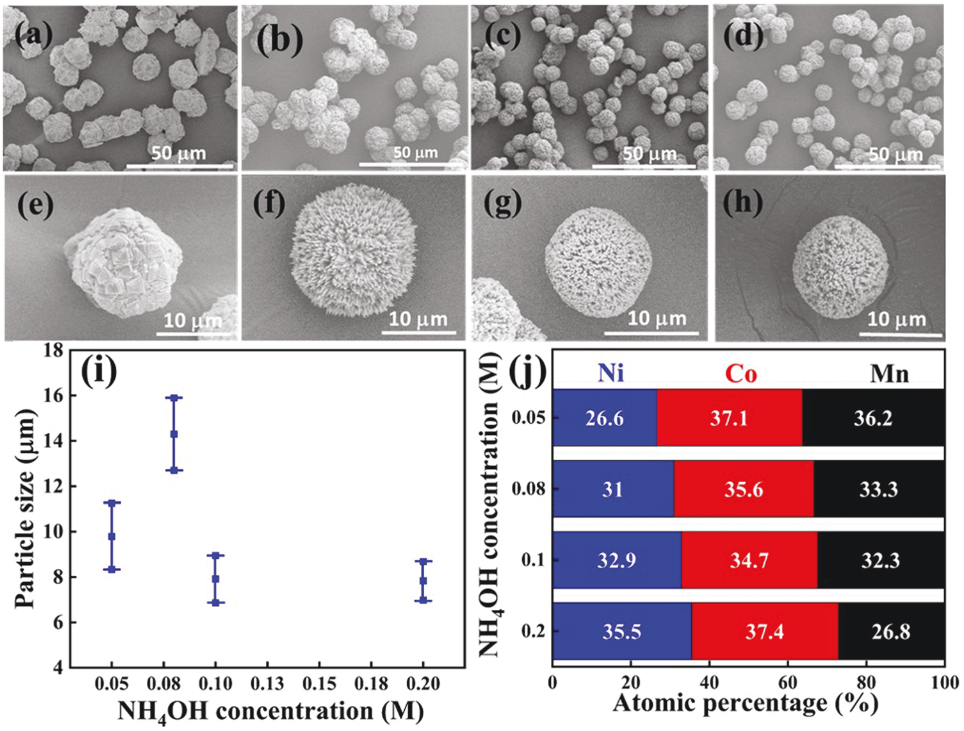

Fig. 4. SEM images of oxalate particles synthesized using different NH_4OH concentrations (a,e) 0.05 M (b,f) 0.08 M (c,g) 0.1 M and (d,h) 0.2 M. (i) Plot showing the effect of variation of NH_4OH concentration on the oxalate particle size; (j) Plot showing the effect on the metal ion composition of the oxalate precursors synthesized using different NH_4OH concentrations (collected from ICP-OES).

(9.8 µm to 14.3 µm). Further increase in the ammonium hydroxide concentration to 0.2 M only resulted in decrease in particle size (14.3 µm to 7.9 µm). The composition of the samples is analyzed using ICP and the results are shown in Fig. 4(j). The amount of nickel in the oxalate precursor increases with increasing the NH_4OH concentration. An opposite trend is observed with manganese as it decreased with increase in the NH_4OH concentration. These two trends are the result of the chelating ability of the Ni^{2+} and Mn^{2+} ions with the amine and oxalate ligands respectively [36]. Manganese generally favors forming a complex with oxalate rather than amine hence NCM(Ox)-0.05 had higher manganese content. NCM(Ox)-0.2 which is prepared using a higher concentration of NH_4OH is more conducive for nickel amine complex formation hence this oxalate precursor had the highest amount of nickel. However, in all the four reaction conditions the cobalt content is the highest in the as-synthesized precursors. The reason is discussed in the Section 3.2.3.

To further study the effect of the NH_4OH concentration on the quality of the slug flow derived NCM111 oxalate produced, three precursor samples were chosen; NCM(Ox)-0.08, NCM(Ox)-0.1 and NCM (Ox)-0.2 for electrochemical testing. As the composition ratios of NCM (Ox)-0.08 and NCM(Ox)-0.2 were not stoichiometric, the compositions of the starting transition metal solutions for both conditions were adjusted so that precursor samples with stoichiometric ratios were obtained. The three precursors were calcined following the procedure in Section 2 and the analysis of the resulting NCM111 is discussed below.

The crystalline structure of three samples were analyzed using XRD and the profiles are displayed in Fig. 5(a). All the peaks are indexed to the hexagonal α-$NaFeO_2$ type structure of the R-3 m space group [9,37]. As no additional peaks are observed in any of the profiles, this indicates there are no phase impurities present in any of the NCM111 samples. Clear splitting of the (006 / 102) and the (108/110) doublets indicate the samples have a well-ordered layered structure. This is further proven with the c/a ratio of the lattice parameters (c and a) obtained via Rietveld refinement, shown in Fig. S4 and values tabulated in Table 2. This ratio indicates the degree of trigonal distortion and since all three samples have a ratio greater than 4.9, they all have a well-defined hexagonal structure [38]. The ratio of the peak intensities of the (003) and (104) planes indicates the extent of cation mixing [39,40]. Here, all the three samples show a ratio greater than 1.2. The amount of Ni^{2+} present in the Li^{+} layer (cation mixing) is calculated using Rietveld refinement. NCM-0.1 had the least amount of cation mixing (2.75%) followed by NCM-0.08 with 2.93% and NCM-0.2 had the highest degree of 2.98%. Morphology analysis of the resulting lithiated samples is conducted using SEM and the images are shown in Fig. 5(b) and Fig. 5(c) for NCM-0.08 and the rest of the samples are shown in Fig. S5. For all three samples, it is observed that the size of the needle shaped primary particles increased after calcination and the spherical morphology was retained using the slow heating rate during the process. Tap density of samples increased after calcination and the NCM-0.08 shows the highest value.

3.2.2. *Effect of residence time on NCM111 particle properties*

Among the various flow parameters, the residence time is directly related to the total reaction time, i.e. the average time spent by the individual slug in the flow reactor. [41,42] Hence, the effect of residence time on the properties of the precursor and lithiated particles and its impact on electrochemical performance is an important aspect of this work. Three different residence times of 2, 4 and 8 minutes are chosen to perform the slug-flow based NCM111 oxalate synthesis. It is observed from the previous section, that the NCM-0.08 shows the highest tap density, which further assures a better electrochemical performance (described in Section 3.3) among the three. Hence, the NH_4OH concentration of 0.08 M is chosen to produce all precursor particles, while varying the residence time. The residence times of the reaction are varied by changing the length of the tubing inside the oven. All three samples had the same particle morphology which consisted of needle shaped primary particles and spherical secondary particles indicating residence time has no effect on particle morphology (Fig. S6). The effect of the residence time on the other particle-properties, including average particle size and composition is displayed in Fig. 6. Increasing the residence time from 2 to 4 minutes led to an increase in particle size from 7.7 μm to 14.3 μm and with further increase in the residence time, particle size decreased to 8.4 μm. Minimal variation in composition is observed at different residence times; however, in all the three cases, again cobalt presents in the highest atomic percent of the total composition. The three samples are lithiated and the XRD patterns of the NCM111 samples are shown in Fig. S7. Data obtained from further analysis of the diffraction patterns is shown in Fig. S8 and Table S1. All three samples had c/a ratios greater than 4.9 indicating they all have a hexagonal structure. The clear splitting of the (006 /102) and (108 / 110) doublets demonstrate the samples contain well-ordered layered structures. The intensity ratios of the (003) and (104) peaks were greater than 1.2, signifying minimal cation mixing. The extent of the cation mixing was determined using Rietveld refinement and NCM-R2 had the least cation mixing of 1.59%, followed by NCM-R4 with 2.93% and NCM-R8 of 3.15%. SEM images in Fig. S9 show the spherical morphology for all three samples is retained after calcination. All three samples had tap densities greater than 1 g ml^{-1}.

Table 2
Cation mixing and lattice parameters from X-ray diffraction patterns with the samples' corresponding particle sizes and tap density values.

Sample Name	a (Å)	c (Å)	V ($Å^3$)	c/a	Ni^{2+} in Li^{+} (%)	Tap density (g ml^{-1})
NCM-0.08	2.846	14.188	99.55	4.985	2.93	1.32
NCM-0.1	2.849	14.196	99.82	4.983	2.75	1.10
NCM-0.2	2.846	14.193	99.58	4.987	2.98	1.16

The oxidation states of the transition elements largely govern the stability and properties of the NCM based cathodes. The XPS analysis was performed on NCM-R2 to get information about the oxidation states (Fig. S10). The high-resolution Ni 2p spectra shows two peaks at 854.39 and 872.26 eV, corresponding to the Ni $2p_{3/2}$ and $2p_{1/2}$, respectively. [43] Both the peaks can be deconvoluted into two peaks indicates toward the presence of Ni^{2+} and Ni^{3+}. The peaks at 854.16 and 872.12 eV are attributed to Ni^{2+} and those are more intense compared to the peaks at 855.43 and 875.85 eV, stands for Ni^{3+}. The difference in intensities indicating towards the predominance of Ni^{2+}. Each of the Ni^{2+} and Ni^{3+} peaks are accompanied with satellite peaks at higher binding energy. In case of Co 2p spectra the $2p_{3/2}$ and $2p_{1/2}$ peaks are observed at 779.3 and 794.4 eV, respectively. [43] A careful deconvolution of the spectra shows that, it is predominantly composed of Co^{3+}, which accompanied by two weak satellite peaks at the higher binding energy of 789.80 and 803.11 eV. The high-resolution Mn 2p spectra, composed of $2p_{3/2}$ at

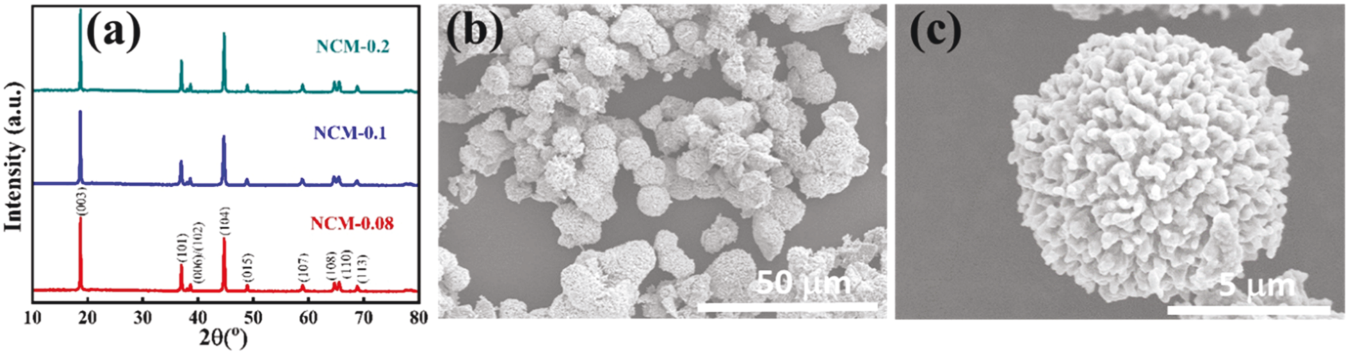

Fig. 5. (a) XRD profiles and (b,c) SEM images of the NCM-0.08 at different magnifications.

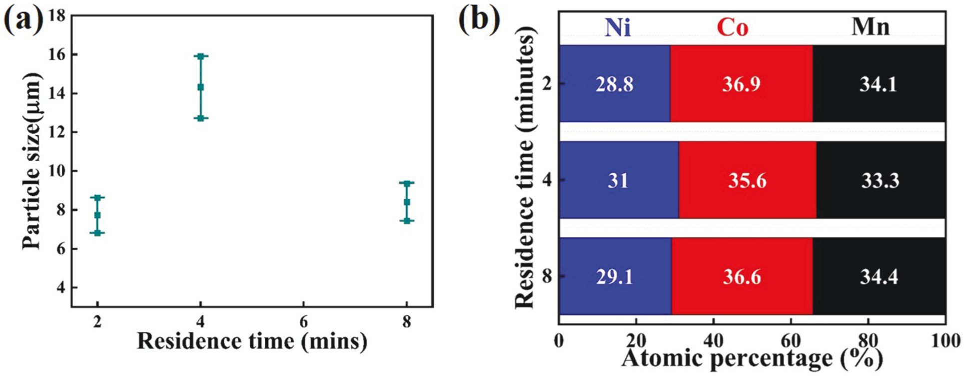

Fig. 6. (a) Plot showing the effect of variation of residence time on the size of oxalate particles; (b) Plot showing the effect of varying the residence time on the metal ion composition of the oxalate precursors (collected from ICP-OES).

641.25 eV and $2p_{1/2}$ at 653 eV, shows a mix-valence of +3 and +4. [43] The O 1 s spectra is deconvoluted in two intense peaks of 528.7 and 531.3 eV, corresponding to the surface oxygen and lattice oxygen, respectively. [43]

3.2.3. Explanation of Co-rich product formation

In both cases (variation of NH_4OH concentration and residence time), it is observed that the precursor particles are Co-rich. One rational way to understand the reason behind this phenomenon is to study the precipitation behavior of the transition metals as oxalates in single and bi-metallic systems. From reported batch oxalate experiments in literature, it is observed that among the three transition elements, nickel is the slowest to precipitate in comparison to cobalt and manganese. [7,27] Using the slug-flow reactor, while keeping similar reaction conditions as those in Section 3.1, single element experiments are carried out. In this case also no nickel oxalate precipitate is formed. Both cobalt and manganese precipitated out of solution, however more cobalt oxalate is formed compared to manganese oxalate. Further study is carried out with bi-metallic oxalate co-precipitation experiments in both reactors with equi-molar metal salts and keeping the reaction conditions comparable. The SEM images of all the bi-metallic oxalates are shown in Fig. S11. The compositions of all the products are analyzed using ICP analysis and given in Fig. 7(a-c). In the case of $Ni_xMn_{1-x}C_2O_4$, the composition of the batch oxalate is close to the target value while the slug flow product is Ni-rich. However, both of the $Ni_xCo_{1-x}C_2O_4$ and $Co_xMn_{1-x}C_2O_4$ contains more cobalt in terms of atomic percentage. From these findings, it can be postulated that as cobalt oxalate readily precipitates out of the solution, it will play the role of the seeding agent during co-precipitation of the tri-metallic oxalate.

3.3. Electrochemical performance

3.3.1. Comparison of electrochemical performance of NCM111 from batch and slug-flow-reactors

The electrochemical performance of batch and slug-flow-derived cathode materials, i.e. NCM_B and NCM_{SF}, respectively (synthesized in similar reaction conditions) are analyzed by charge-discharge analysis within the voltage window of 2.7 – 4.3 V (versus Li/Li^+), shown in Fig. 8. Although, the NCM_B has slightly better capacitive performance at 0.1 C (Fig. 8a), a greater charge−discharge plateau gap is observed compared to the NCM_{SF}, indicating the greater polarizability of the former one. Fig. 8(b) demonstrates the rate capability of both the cathodes and the charge-discharge profiles are shown in Fig. S12. It is interesting to notice that the two materials show comparative capacitive performance at lower C-rates (0.1 C and 0.2 C); however, NCM_{SF} outperforms NCM_B at higher C-rates (0.5 – 2 C), indicating a better rate capability. Lesser polarizability of NCM_{SF}–based cathode signifies a higher structural robustness upon chare-discharge. Better capacitive performance of NCM_{SF} at higher C-rates further confirms the better ability to withstand the fast intercalation/de-intercalation of Li^+ ions into the layered structure at higher C-rates. The superior structural stability of the NCM_{SF} can be attributed to the higher tap density, particle size uniformity, and morphological homogeneity at both the precursor and lithiated states compared to NCM_B.

3.3.2. Electrochemical performance of slug-flow-derived NCM111 with varying NH_4OH concentrations and residence times

(a) Effect of NH_4OH concentration: It is already established in the previous section that the NH_4OH concentration plays a crucial role in determining the particle size of the precursor, which finally controls the particle size of the final lithiated materials. Another important performance determining parameter of the lithiated material is the percent of Ni^{2+}/Li^+ mixing which affects the structural robustness and Li^+ diffusion kinetics of the cathode material. From the charge-discharge profile

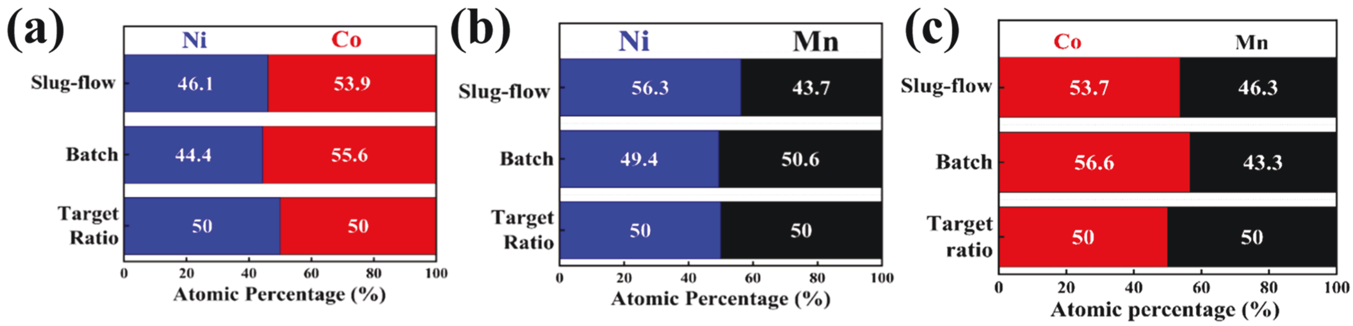

Fig. 7. Atomic percentage of the elements calculated from ICP-OES analysis for (a) $Ni_xCo_{(1-x)}C_2O_4$ and (b) $Ni_xMn_{(1-x)}C_2O_4$ and (c) $Co_xMn_{(1-x)}C_2O_4$.

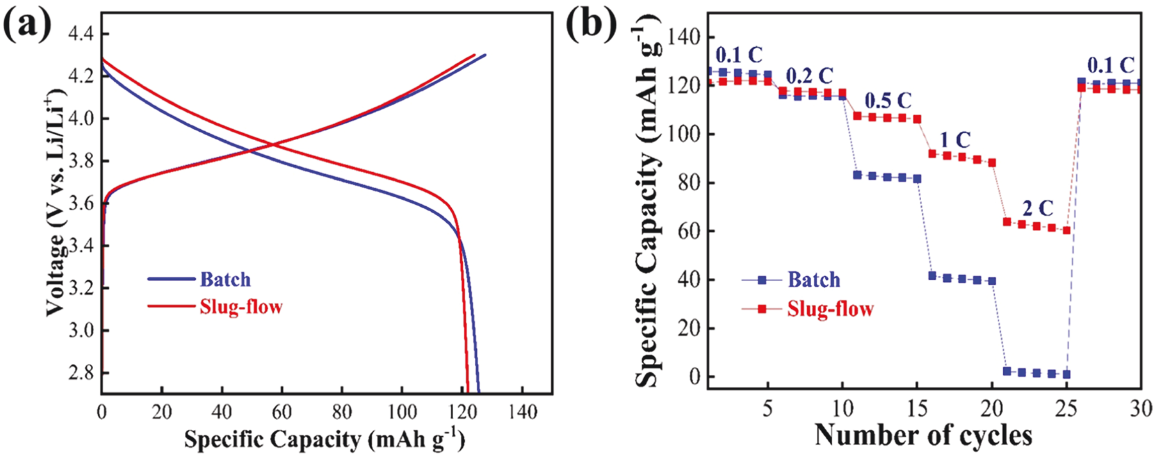

Fig. 8. (a) Charge-discharge at 0.1 C and (b) Rate capability plot at different c-rates of the lithiated batch and slug-flow derived materials.

at lower C-rate (at 0.1 C) it is observed that, the NCM-0.1 is showing the highest specific capacity of 122 mAh g^{-1} (Fig. S13a), whereas NCM-0.08 and NCM-0.2 achieve specific capacities of 118 and 110 mAh g^{-1}, respectively. The high initial specific capacity of the NCM-0.1 can be attributed to the lower extent of cation mixing (Table 2) in the pristine material. It is well known that, the Li^+ storage behavior of a cathode largely depends on the charging rate of the battery. [44] Hence, the charge-discharge profiles of all the three materials within the voltage window of 2.7–4.3 V (vs. Li/Li^+) at different C-rates are included in Fig. S14 and the corresponding rate capability plots are shown in Fig. S13(b). It is interesting to notice from the rate capability plots that although the NCM-0.1 is the highest performing material at lower C rates (up to 0.5 C), its capacity fading rate is higher with increasing the C-rate up to 2 C, leading to the worst rate capability among the three. From the rate capability plot it is calculated that cathode materials; NCM-0.08, NCM-0.1 and NCM-0.2 retain 63%, 50% and 54% of initial specific capacity respectively at a higher C-rate of 2 C (Fig. S13b). The higher rate capability of NCM-0.08 with the highest tap density is ascribed to the high structural stability of its secondary particles at higher C-rate. The cycling performance of the three materials is also evaluated both at lower (0.5 C) and higher (1 C) C-rates. From Fig. S13 (c), it is observed that NCM-0.08 and NCM-0.1 show higher capacity retention of >85% with the columbic efficiency of >95% at the end of the 100 charge discharge cycles at 0.5 C. On the other hand, NCM-0.2 shows a lower capacity retention of 71%. In order to understand the reason behind the observed trend in cycling performance the differential capacity (dQ/dV) analysis was performed for all three cathode materials after 2nd, 50th and 100th cycles (Fig. S13d, e, f). In all the cases the dQ/dV plots consist of one pair of redox peaks, corresponding to Li^+ de-intercalation upon charging and Li^+ intercalation upon discharging, which is obvious for NCM111 based cathodes. A careful analysis of the dQ/dV plots reveals that there is a small change in the peak positions in the case of NCM-0.08 and NCM-0.1 upon cycling, whereas a significant shift in peak positions is observed for the NCM-0.2 based LIB. This indicates a severe electrode polarization for NCM-0.2 at lower C-rates, resulting towards the decrease of capacitive performance in a higher extent. The effect of consecutive potential induced Li^+ intercalation/de-intercalation to/from cathode is further analyzed by the impedance analysis during the various stages of cycling at 0.5 C. The Nyquist plots (Fig. S13g, h and i) are fitted with suitable equivalent circuit (Fig. S15), consisting of R_f (surface resistance), R_{ct} (charge-transfer resistance), CPE 1 and CPE 2 (constant phase elements) and W (Warburg impedance). The R_f and R_{ct} show similar trend of increasing, whereas the W values show a decreasing trend upon cycling for all the three cases. The Li^+ diffusion co-efficient values are calculated based on the W values. The fitted parameters are shown in Table S2. It is observed that in terms of R_f and R_{ct}, NCM-0.2 has the lowest values and the Li^+ diffusion co-efficient shows the highest values at every stages of cycling. This is probably due to the smaller particle size, which offers more Li^+ diffusion channels throughout the material. However, the extent of decrease of D_{Li+} at every stage of cycling are higher for NCM-0.2, which indicates more structural pulverization of the material probably due to the parasitic side reactions caused by the higher exposure to the electrolyte. On the other hand, although NCM-0.08 shows lower value of initial D_{Li+}, the extent of decrease of that value is also less. This ensures a better capacity retention after 100 cycles at 0.5 C. This can be ascribed to the lesser exposure of the secondary particles to the electrolyte caused by the bigger particle size. The cycling performance at higher C-rate of 1 C shows an opposite trend of capacity retention for NCM-0.1 and NCM-0.2 (Fig. S16). In this case, NCM-0.1 shows the poorest capacity retention of 35% and NCM-0.2 shows the highest capacity retention of 66% after 100 cycles. In order to understand the reason behind the capacity decay after cycling, post-cycling SEM analysis was performed. The secondary particles of NCM-0.1 were found to lose their structural integrity after cycling while secondary particles of NCM-0.08 and NCM-0.2 retained most of their structural integrity (Fig. S17).

(b) Effect of residence time: After comparing all the results from the cathode materials synthesized using different NH_4OH concentration, NCM-0.08 shows a perfect trade-off between the specific capacity and cycling performance both at lower and higher C-rates. It has the highest secondary particle size, narrower particle size distribution and highest tap density, indicating better structural integrity for facile Li^+ diffusion kinetics which is a factor attributed to good electrochemical performance. Hence, the NH_4OH concentration of 0.08 M is chosen to produce the precursor particles for the optimization of residence time. Fig. 9 shows the electrochemical performance of the lithiated NCM111 produced using different residence times. Significant difference between the electrochemical performances are observed for the three lithiated materials. From the charge discharge plot of 0.1 C (Fig. 9a) it is observed that the NCM-R2 achieves the highest specific capacity of 128 mAh g^{-1}. The rate capability of the material is also better compared to the other two materials with retention of 67% at 2 C. On the other hand, NCM-R8 shows the worst performance in terms of both specific capacity and rate capability (Fig. 9a and b). Charge-discharge profiles of all the three materials at different C-rates are included in Fig. S18. From the cycling stability analysis of 100 cycles at 0.5 C, the capacity retention values calculated are 85%, 88% and 69% for NCM-R2, NCM-R4 and NCM-R8, respectively. Corresponding dQ/dV plots further justify the trend of cycling performance (Fig. 9d, e and f). It is observed that, NCM-R2 and NCM-R4 show less electrode polarization upon cycling, whereas there is a huge electrode polarization observed for the NCM-R8 material. The impedance analysis (Fig. 9g, h and i) provides further insight into the

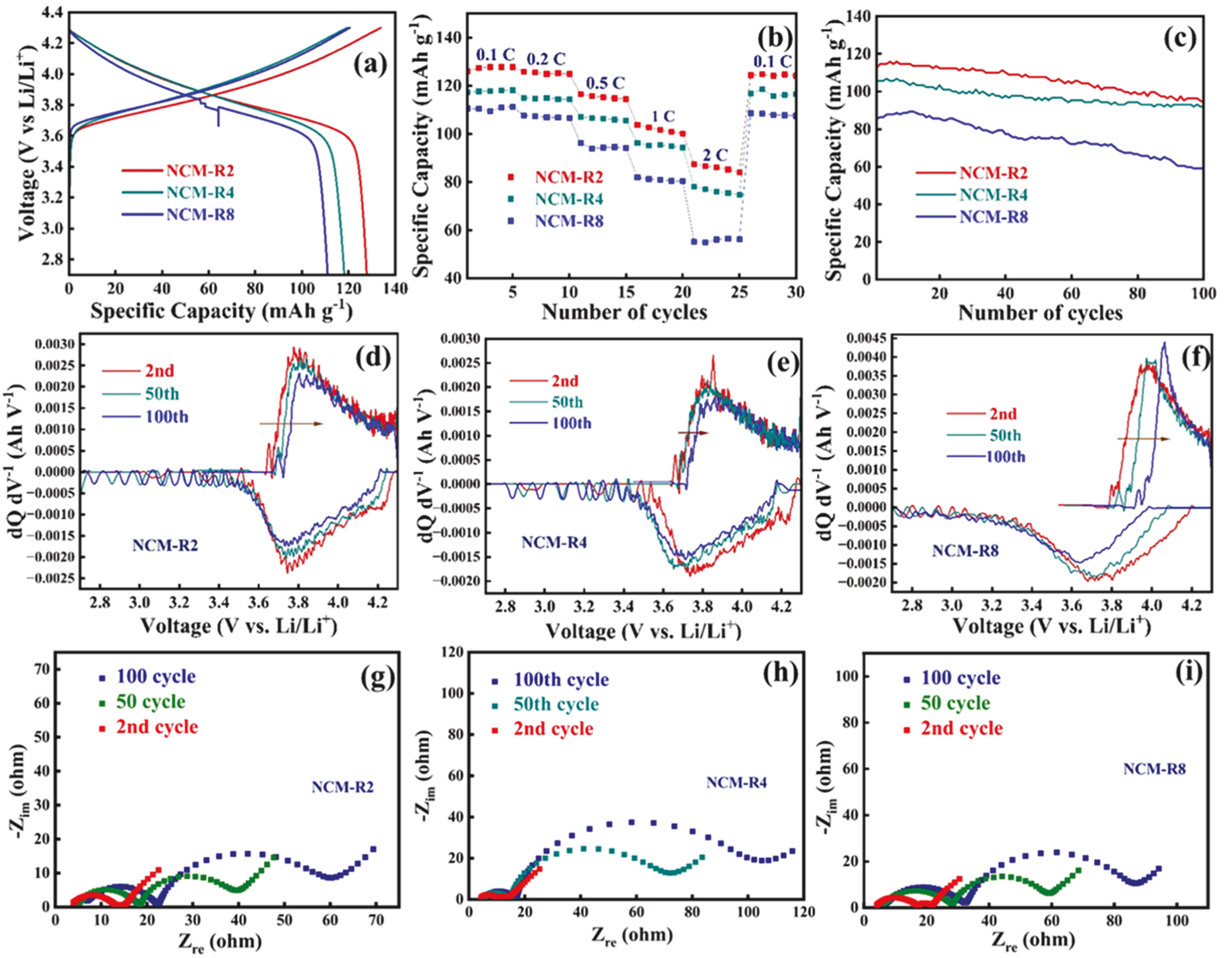

Fig. 9. (a) Charge-discharge at 0.1 C (b) rate capability and (c) cycling performance at 0.5 C of lithiated NCM-R2, NCM-R4 and NCM-R8. dQ/dV and Nyquist plots after 2nd, 50th and 100th cycle for (d, g) NCM-R2, (e, h) NCM-R4 and (f, i) NCM-R8 are shown.

variation in electrochemical behavior of the cathodes upon cycling. The fitted values are shown in the supporting information, Table S3. After fitting the Nyquist plot with suitable equivalent circuit, it is observed that, NCM-R2 shows the least charge transfer (R_{ct}) resistance at each of the stages of cycling up to 100 cycles at 0.5 C. Although the D_{Li+} shows a decreasing trend, it is higher for NCM-R2 at each stage of cycling compared to the other two materials, indicating towards more facile Li^+ diffusion kinetics. The cycling performance of the three materials is also checked at 1 C and shown in Fig. S19. Post cycling SEM images (Fig. S20) shows a better retention of initial particle morphology for NCM-R2 compared to the other two materials after 100 cycles at 1 C. Hence, it can be concluded that the NH_4OH concentration of 0.08 M and a residence time of 2 min. is the optimum condition for the slug-flow synthesis of NCM111 oxalate precursors followed by calcination at slower heating rate to retain its morphological integrity. A comparison table is made based on the particle nature and the electrochemical performance of the NCM-R2 with the already reported NCM111 derived from stirred tank-based reactors (Table S4).

4. Conclusion

In this work, slug flow-based continuous manufacturing is successfully utilized to synthesize nickel cobalt manganese oxalate precursors using co-precipitation chemistry and then lithiated to produce final NCM111 cathode for electrochemical analysis. The work is unique in various aspects and the key findings are listed as follows: (i) From the comparative study, it is observed that the oxalate derived from the slug flow reactor had better homogeneity in terms of PSD and morphology (spherical) and also achieves higher tap density in comparison to the batch-derived oxalate. (ii) The precipitation behavior of the three transition metals in the slug-flow set up is studied systematically and cobalt oxalate is found to act as the seeding agent that facilitates the precipitation of other two elements during NCM-oxalate formation. (iii) The effect of the variation of NH_4OH concentration and residence time on the particle quality are evaluated to optimize the chemical and flow parameters to produce the best quality precursor. It can be concluded that the NH_4OH concentration plays an important role in determining the elemental composition and particle size, whereas residence time primarily influences the secondary particle size. (iv) A slow heating rate can be utilized during the lithiation step to retain the spherical morphology of the cathode materials. (v) The electrochemical analysis shows that slug-slow derived NCM has better rate capability and structural stability compared to the batch-derived product. (vi) NCM111 synthesized, using NH_4OH concentration of 0.08 M and a residence time of 2 minutes had the best electrochemical performance in terms of specific capacity, cycling stability and Li^+ diffusion kinetics compared to the other materials. The stepwise demonstration of the optimization of slug-flow parameters combined with the evaluation of electrochemical performances of the respective NCM111s is a unique aspect of this work and it will provide a better understanding on continuous manufacturing of NCM-based cathodes.

CRediT authorship contribution statement

Jethrine H. Mugumya: Writing – original draft, Validation, Software, Methodology, Investigation, Formal analysis, Data curation. **Sourav Mallick:** Writing – review & editing, Visualization, Software, Investigation, Formal analysis, Data curation. **Arjun Patel:** Writing – review & editing, Software, Data curation. **Michael L. Rasche:** Writing – review & editing, Software. **Aardra V. Sakpal:** Data curation. **Ethan D. Huchler:** Data curation. **Sunuk Kim:** Data curation. **Mo Jiang:** Writing – review & editing, Supervision, Project administration, Funding acquisition, Conceptualization. **Ram B. Gupta:** Supervision, Funding acquisition, Conceptualization.

Declaration of Competing Interest

The authors declare that they have no known competing financial interests or personal relationships that could have appeared to influence the work reported in this paper.

Data Availability

All the data is included in the manuscript and supporting information documents

Acknowledgement

This material is based upon work supported by Virginia Commonwealth University and the National Science Foundation (Grant No. CMMI-1940948) and U.S. Department of Energy, Office of Energy Efficiency and Renewable Energy, Advanced Materials and Manufacturing Technologies Office (award DE-EE0009110). Mingyao Mou and Sophie Kothie are acknowledged for providing the slug flow co-precipitation technology developed in Mo Jiang Lab.

Appendix A. Supporting information

Supplementary data associated with this article can be found in the online version at doi:10.1016/j.jallcom.2024.174720.

References

[1] J. Wang, P. Nie, B. Ding, S. Dong, X. Hao, H. Dou, X. Zhang, Biomass Derived Carbon for Energy Storage Devices. (2017). https://doi.org/10.1039/c6ta08742f.

[2] L. Mauler, F. Duffner, J. Leker, Economies of scale in battery cell manufacturing: the impact of material and process innovations, Appl. Energy *286* (2021) 116499, https://doi.org/10.1016/j.apenergy.2021.116499.

[3] S. Mallick, A. Patel, X.-G. Sun, M. Parans, M. Mou, J.H. Mugumya, M. Jiang, M. L. Rasche, H. Lopez, R.B. Gupta, Low-cobalt active cathode materials for high-performance lithium-ion batteries: synthesis and performance enhancement methods, J. Mater. Chem. A *11* (2023) 3789–3821, https://doi.org/10.1039/d2ta08251a.

[4] B.E. Murdock, K.E. Toghill, N. Tapia-Ruiz, A perspective on the sustainability of cathode materials used in lithium-ion batteries, Adv. Energy Mater. *11* (2021), https://doi.org/10.1002/aenm.202102028.

[5] S. Ahmed, P.A. Nelson, K.G. Gallagher, N. Susarla, D.W. Dees, Cost and energy demand of producing nickel manganese cobalt cathode material for lithium ion batteries, J. Power Sources *342* (2017) 733–740, https://doi.org/10.1016/J.JPOWSOUR.2016.12.069.

[6] N. Muralidharan, E.C. Self, M. Dixit, Z. Du, R. Essehli, R. Amin, J. Nanda, I. Belharouak, Next-Generation Cobalt-Free Cathodes-A Prospective Solution to the Battery Industry's Cobalt Problem. (2022). https://doi.org/10.1002/aenm.202103050.

[7] H. Dong, G.M. Koenig, Compositional control of precipitate precursors for lithium-ion battery active materials: role of solution equilibrium and precipitation rate, J. Mater. Chem. A *5* (26) (2017) 13785–13798, https://doi.org/10.1039/c7ta03653a.

[8] D. Wang, I. Belharouak, L.H. Ortega, X. Zhang, R. Xu, D. Zhou, G. Zhou, K. Amine, Synthesis of high capacity cathodes for lithium-ion batteries by morphology-tailored hydroxide co-precipitation, J. Power Sources *274* (2015) 451–457, https://doi.org/10.1016/j.jpowsour.2014.10.016.

[9] S.H. Park, S.H. Kang, I. Belharouak, Y.K. Sun, K. Amine, Physical and electrochemical properties of spherical $Li_{1+x}(Ni_{1/3}Co_{1/3}Mn_{1/3})_{1-x}O_2$ cathode materials, J. Power Sources *177* (1) (2008) 177–183, https://doi.org/10.1016/J.JPOWSOUR.2007.10.062.

[10] Q. Zhu, H. Xiao, R. Zhang, S. Geng, Q. Huang, Effect of impeller type on preparing spherical and dense $Ni_{1-x-y}Co_xMn_y(OH)_2$ precursor via continuous co-precipitation in pilot scale: a case of $Ni_{0\cdot6}Co_{0\cdot2}Mn_{0\cdot2}(OH)_2$, Electrochim. Acta *318* (2019) 1–13, https://doi.org/10.1016/J.ELECTACTA.2019.06.008.

[11] W. Hua, W. Liu, M. Chen, S. Indris, Z. Zheng, X. Guo, M. Bruns, T.H. Wu, Y. Chen, B. Zhong, S. Chou, Y.M. Kang, H. Ehrenberg, Unravelling the growth mechanism of hierarchically structured $Ni_{1/3}Co_{1/3}Mn_{1/3}(OH)_2$ and their application as precursors for high-power cathode materials, Electrochim. Acta *232* (2017) 123–131, https://doi.org/10.1016/j.electacta.2017.02.105.

[12] Z. Zheng, X.D. Guo, S.L. Chou, W.B. Hua, H.K. Liu, S.X. Dou, X.S. Yang, Uniform Ni-Rich $LiNi_{0.6}Co_{0.2}Mn_{0.2}O_2$ porous microspheres: facile designed synthesis and their improved electrochemical performance, Electrochim. Acta *191* (2016) 401–410, https://doi.org/10.1016/j.electacta.2016.01.092.

[13] J.G. Costandy, T.F. Edgar, M. Baldea, Switching from batch to continuous reactors is a trajectory optimization problem, Ind. Eng. Chem. Res. *58* (30) (2019) 13718–13736, https://doi.org/10.1021/acs.iecr.9b01126.

[14] K. Plumb, Continuous processing in the pharmaceutical industry: changing the mind set, Chem. Eng. Res. Des. *83* (6) (2005) 730–738, https://doi.org/10.1205/CHERD.04359.

[15] M. Jiang, Z. Zhu, E. Jimenez, C.D. Papageorgiou, J. Waetzig, A. Hardy, M. Langston, R.D. Braatz, Continuous-Flow Tubular Crystallization in Slugs Spontaneously Induced by Hydrodynamics. (2014) https://doi.org/10.1021/cg401715e.

[16] F.A. Holland, R. Bragg, Gas–liquid two-phase flow, Fluid Flow. Chem. Eng. (1995) 219–267, https://doi.org/10.1016/B978-034061058-9.50009-8.

[17] S. Mokhatab, W.A. Poe, Raw gas transmission, Handb. Nat. Gas. Transm. Process. (2012) 85–180, https://doi.org/10.1016/B978-0-12-386914-2.00003-0.

[18] M. Mou, A. Patel, S. Mallick, B.P. Thapaliya, P. Paranthaman, J.H. Mugumya, M. L. Rasche, R.B. Gupta, S. Saleh, S. Kothe, E. Baral, G.P. Pandey, H. Lopez, M. Jiang, Scalable advanced $Li(Ni_{0.8}Co_{0.1}Mn_{0.1})O_2$ cathode materials from a slug flow continuous process, ACS Omega *7* (2022) 42408–42417, https://doi.org/10.1021/acsomega.2c05521.

[19] M. Jiang, R.D. Braatz, Designs of continuous-flow pharmaceutical crystallizers: developments and practice, CrystEngComm *21* (2019) 3534, https://doi.org/10.1039/c8ce00042e.

[20] M.H. Lee, Y.J. Kang, S.T. Myung, Y.K. Sun, Synthetic optimization of $Li[Ni_{1/3}Co_{1/3}Mn_{1/3}]O_2$ via Co-Precipitation, Electrochim. Acta *50* (4) (2004) 939–948, https://doi.org/10.1016/j.electacta.2004.07.038.

[21] J.H. Mugumya, M.L. Rasche, R.F. Rafferty, A. Patel, S. Mallick, M. Mou, J.A. Bobb, R.B. Gupta, M. Jiang, Synthesis and theoretical modeling of suitable co-precipitation conditions for producing NMC111 cathode material for lithium-ion batteries, Energy Fuels (2022), https://doi.org/10.1021/acs.energyfuels.2c01805.

[22] T.H. Cho, Y. Shiosaki, H. Noguchi, Preparation and characterization of layered $LiMn_{1/3}Ni_{1/3}Co_{1/3}O_2$ as a cathode material by an oxalate co-precipitation method, J. Power Sources *159* (2) (2006) 1322–1327, https://doi.org/10.1016/j.jpowsour.2005.11.080.

[23] Y. Zhu, J. You, H. Huang, G. Li, W. Zhou, J. Guo, Facile synthesis and electrochemical properties of layered $Li[Ni_{1/3}Mn_{1/3}Co_{1/3}]O_2$ as cathode materials for lithium-ion batteries, Front. Mater. Sci. *11* (2) (2017) 155–161, https://doi.org/10.1007/s11706-017-0374-z.

[24] X. Yao, Z. Xu, Z. Yao, W. Cheng, H. Gao, Q. Zhao, J. Li, A. Zhou, Oxalate co-precipitation synthesis of $LiNi_{0.6}Co_{0.2}Mn_{0.2}O_2$ for low-cost and high-energy lithium-ion batteries, Mater. Today Commun. *19* (2019) 262–270, https://doi.org/10.1016/J.MTCOMM.2019.02.001.

[25] T. Zeng, C. Zhang, An effective way of co-precipitating Ni^{2+}, Mn^{2+} and Co^{2+} by using ammonium oxalate as Precipitant for Ni-Rich Li-ion batteries cathode, J. Mater. Sci. *55* (25) (2020) 11535–11544, https://doi.org/10.1007/s10853-020-04753-w.

[26] H. Tian, N. Ye, D. Liu, W. Li, Effects of synthesis conditions on the structural and electrochemical properties of layered $LiNi_{1/3}Co_{1/3}Mn_{1/3}O_2$ cathode material via oxalate co-precipitation method, Rare Met. *27* (6) (2008) 575–579, https://doi.org/10.1016/S1001-0521(08)60185-0.

[27] V.D. Thao, L.T. Son, N.T. Lan, M.N. Huyen, T.T. Nguyen, S.D. Le, P.M. Thao, T. Van Nguyen, Facile synthesis of mixed nickel-cobalt oxalates with composition control as high-performance electrode materials for supercapacitor, J. Energy Storage *66* (2023) 107428, https://doi.org/10.1016/J.EST.2023.107428.

[28] M. Mou, A. Patel, S. Mallick, K. Jayanthi, X.-G. Sun, P. Paranthaman, S. Kothe, E. Baral, S. Saleh, J.H. Mugumya, M.L. Rasche, R.B. Gupta, H. Lopez, M. Jiang, Slug flow coprecipitation synthesis of uniformly-sized oxalate precursor microparticles for improved reproducibility and tap density of $Li(Ni_{0.8}Co_{0.1}Mn_{0.1})O_2$ cathode materials, ACS Appl. Energy Mater. *6* (2023) 3213–3224, https://doi.org/10.1021/acsaem.2c03563.

[29] J. Thati, Å.C. Rasmuson, On the mechanisms of formation of spherical agglomerates, Eur. J. Pharm. Sci. *42* (4) (2011) 365–379, https://doi.org/10.1016/J.EJPS.2011.01.001.

[30] M. Jiang, C.D. Papageorgiou, J. Waetzig, A. Hardy, M. Langston, R.D. Braatz, Indirect ultrasonication in continuous slug-flow crystallization, Cryst. Growth Des. (No. 15) (2015) 2486–2492, https://doi.org/10.1021/acs.cgd.5b00263.

[31] K.A. Berglund, Analysis and measurement of crystallization utilizing the population balance, Handb. Ind. Cryst. (2002) 101–113, https://doi.org/10.1016/B978-075067012-8/50006-9.

[32] M.N. Kashid, I. Gerlach, S. Goetz, J. Franzke, J.F. Acker, F. Platte, D.W. Agar, S. Turek, Internal Circulation within the Liquid Slugs of a Liquid-Liquid Slug-Flow Capillary Microreactor. (2005) https://doi.org/10.1021/ie0490536.

[33] X. Yang, D. Acevedo, A. Mohammad, N. Pavurala, H. Wu, A.L. Brayton, R.A. Shaw, M.J. Goldman, F. He, S. Li, R.J. Fisher, T.F. O'connor, C.N. Cruz, Risk considerations on developing a continuous crystallization system for carbamazepine 21 (7) (2017) 1021–1033, https://doi.org/10.1021/acs.oprd.7b00130.

[34] M. Su, Y. Gao, Air−Liquid Segmented Continuous Crystallization Process Optimization of the Flow Field, Growth Rate, and Size Distribution of Crystals. (2018) https://doi.org/10.1021/acs.iecr.7b05236.

[35] M. Mou, L. dela Rosa, J.H. Mugumya, M. Jiang, ContinuouS Generation of Gas-water Slugs with Improved Size Uniformity at A Tunable Scale, Chem. Eng. Technol. (2023), https://doi.org/10.1002/ceat.202200103.

[36] L. Xu, P. Hou, Y. Zhang, H. Zhang, D. Song, X. Shi, X. Wang, L. Zhang, Carbonate coprecipitation preparation of Li-rich layered oxides using the oxalate anion ligand as high-energy, high-power and durable cathode materials for lithium-ion batteries, J. Mater. Chem. A *3* (42) (2015) 21219–21226, https://doi.org/10.1039/c5ta04157k.

[37] S. Kim, S. Park, M. Jo, M. Beak, J. Park, G. Jeong, J.S. Yu, K. Kwon, Electrochemical effects of residual Al in the resynthesis of $Li[Ni_{1/3}Mn_{1/3}Co_{1/3}]O_2$ cathode materials, J. Alloy. Compd. *857* (2021) 157581, https://doi.org/10.1016/j.jallcom.2020.157581.

[38] Y.L. Xie, L.F. Guo, Preparation and electrochemical performance of $LiNi_{1/3}Co_{1/3}Mn_{1/3}O_2/Li_2FeSiO_4/C$ composites for lithium-ion batteries, J. Alloy. Compd. *925* (2022), https://doi.org/10.1016/j.jallcom.2022.166692.

[39] J.Z. Kong, X.Y. Yang, H.F. Zhai, C. Ren, H. Li, J.X. Li, Z. Tang, F. Zhou, Synthesis and Electrochemical Properties of Li-Excess $Li_{1+x}[Ni_{0.5}Co_{0.2}Mn_{0.3}]O_2$ cathode materials using ammonia-free chelating agent, J. Alloy. Compd. *580* (2013) 491–496, https://doi.org/10.1016/J.JALLCOM.2013.06.149.

[40] H. Wang, Y. Wei, J. Wang, D. Long, Polymer-chelation synthesis of compositionally Homogeneous $LiNi_{1/3}Co_{1/3}Mn_{1/3}O_2$ crystals for lithium-ion cathode, Electrochim. Acta *269* (2018) 724–732, https://doi.org/10.1016/J.ELECTACTA.2018.03.029.

[41] M. Seenivasan, C.C. Yang, S. huang Wu, W.C. Chien, Y.S. Wu, R. Jose, S.J. Lue, Using a Couette–Taylor vortex flow reactor to prepare a uniform and highly stable $Li[Ni_{0\cdot 80}Co_{0\cdot 15}Al_{0.05}]O_2$ Cathode Material, J. Alloy. Compd. *857* (2021), https://doi.org/10.1016/j.jallcom.2020.157594.

[42] D.K. Thai, Q.P. Mayra, W.S. Kim, Agglomeration of Ni-rich hydroxide crystals in Taylor vortex flow, Powder Technol. *274* (2015) 5–13, https://doi.org/10.1016/j.powtec.2015.01.008.

[43] L. Li, L. Wang, X. Zhang, M. Xie, F. Wu, R. Chen, Structural and electrochemical study of hierarchical $LiNi_{1/3}Co_{1/3}Mn_{1/3}O_2$ cathode material for lithium-ion batteries, ACS Appl. Mater. Interfaces *7* (39) (2015) 21939–21947, https://doi.org/10.1021/acsami.5b06584.

[44] Y.N. Zhou, J.L. Yue, E. Hu, H. Li, L. Gu, K.W. Nam, S.M. Bak, X. Yu, J. Liu, J. Bai, E. Dooryhee, Z.W. Fu, X.Q. Yang, High-rate charging induced intermediate phases and structural changes of layer-structured cathode for lithium-ion batteries, Adv. Energy Mater. *6* (21) (2016) 1–8, https://doi.org/10.1002/aenm.201600597.